Supporting Information

New types of open-framework vanadium borophosphates with photocatalytic properties

Yiyao Wang, Xing Liu, Jian Zhou and Hua-Hong Zou

The determination of heavy metal release

After the photo-degradation, the concentrations of heavy metal ions (Cd^{2+} for **1**, Mn^{2+} for **2** and Co^{2+} for **3**) were detected by ICP-OES determination. Standard solutions are prepared by dissolving heavy metal ions at concentrations of 6.66, 13.33, 33.33, 66.66, and 100 μg/L in either RhB or MB solutions, serving as references for calibration. Subsequently, the solutions of RB or MB that have undergone photocatalytic breakdown by compounds **1**-**3** are filtered, with the resultant clear solutions designated as the test samples. Furthermore, uncontaminated RB and MB solutions are utilized as blank controls. The ICP-OES instrument is then employed to establish the relationship between intensity and concentration for both the blank and standard solutions. Through fitting the collected data points, a trend line and its corresponding equation are derived, with the condition that the coefficient of determination ($R^2 \geq 0.999$). Thereafter, the absorption intensities of specific elements—Cd at 214.439 nm, Mn at 259.372 nm, and Co at 238.892 nm—are measured within the test solutions. By applying the obtained trend line equation, the concentrations of these elements in the test samples are accurately computed.

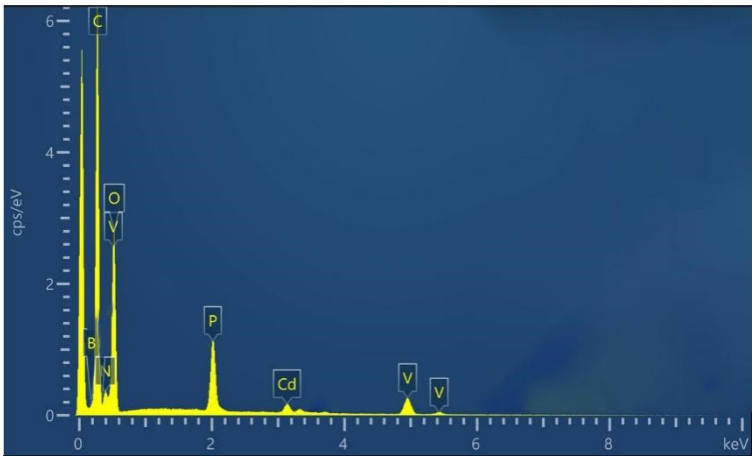

Fig. S1. EDX spectrum of **1**.

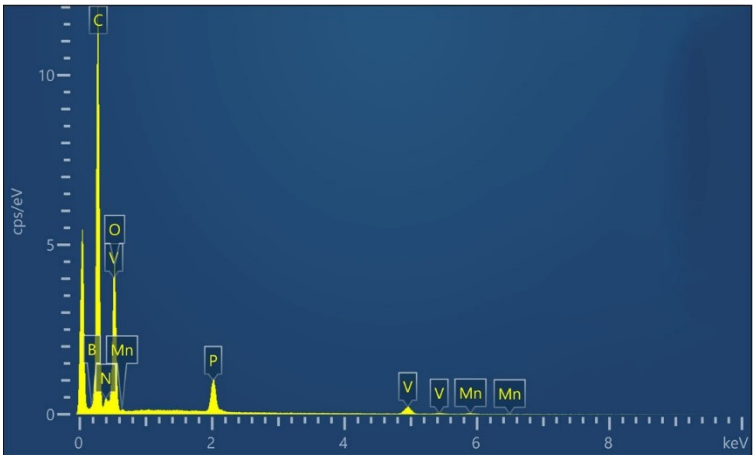

Fig. S2. EDX spectrum of **2**.

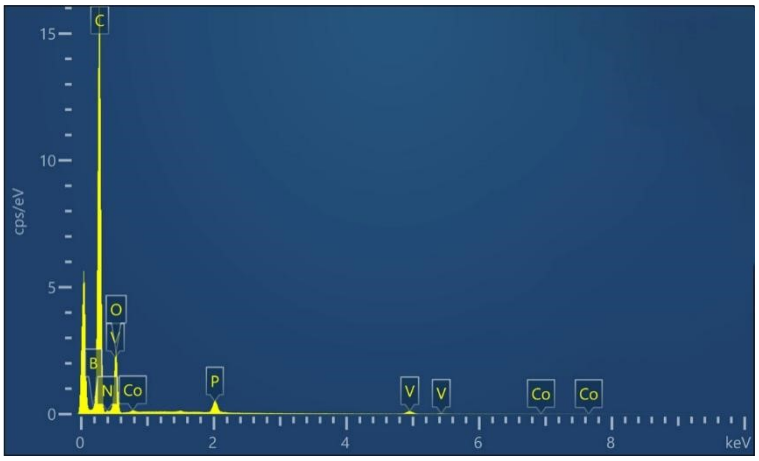

Fig. S3. EDX spectrum of **3**.

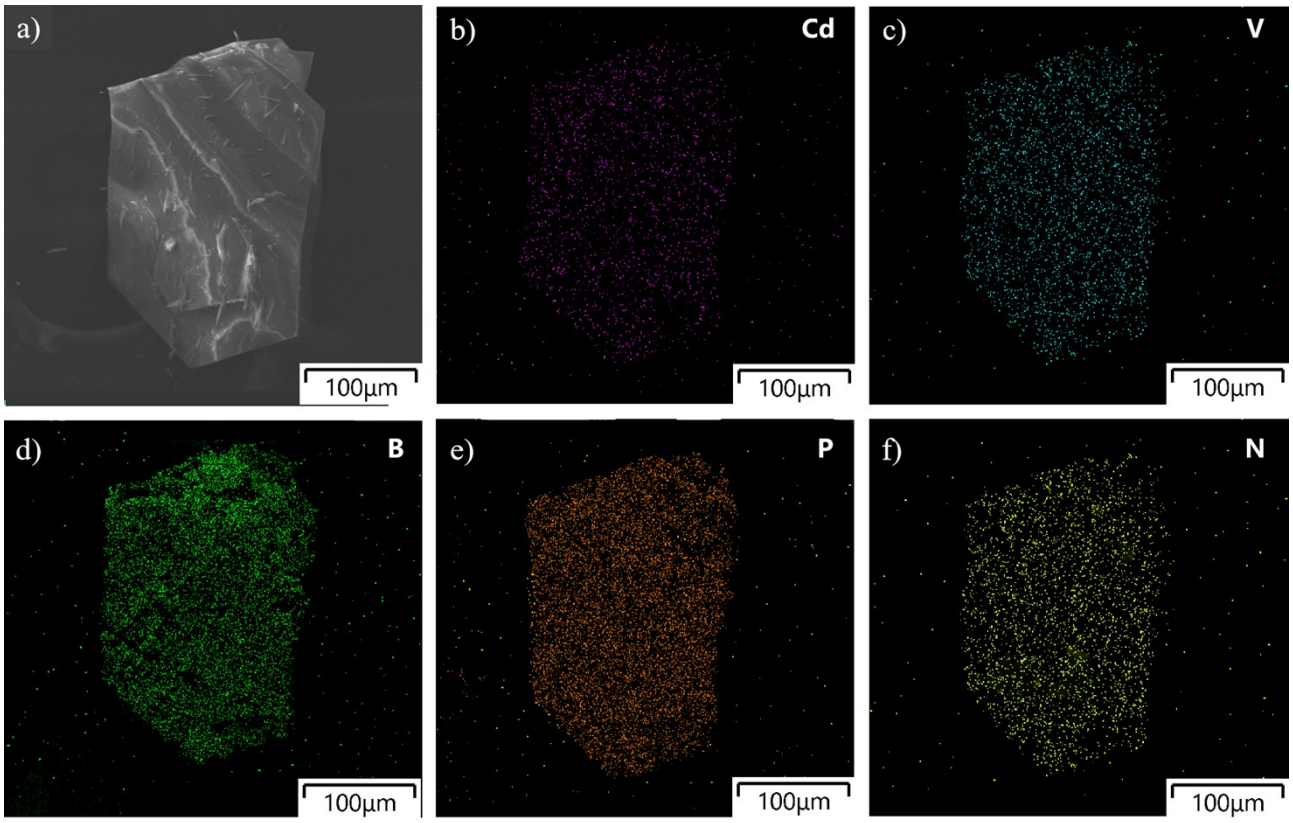

Fig. S4 (a) SEM micrograph image of **1**. (b-f) EDX mapping images of **1**.

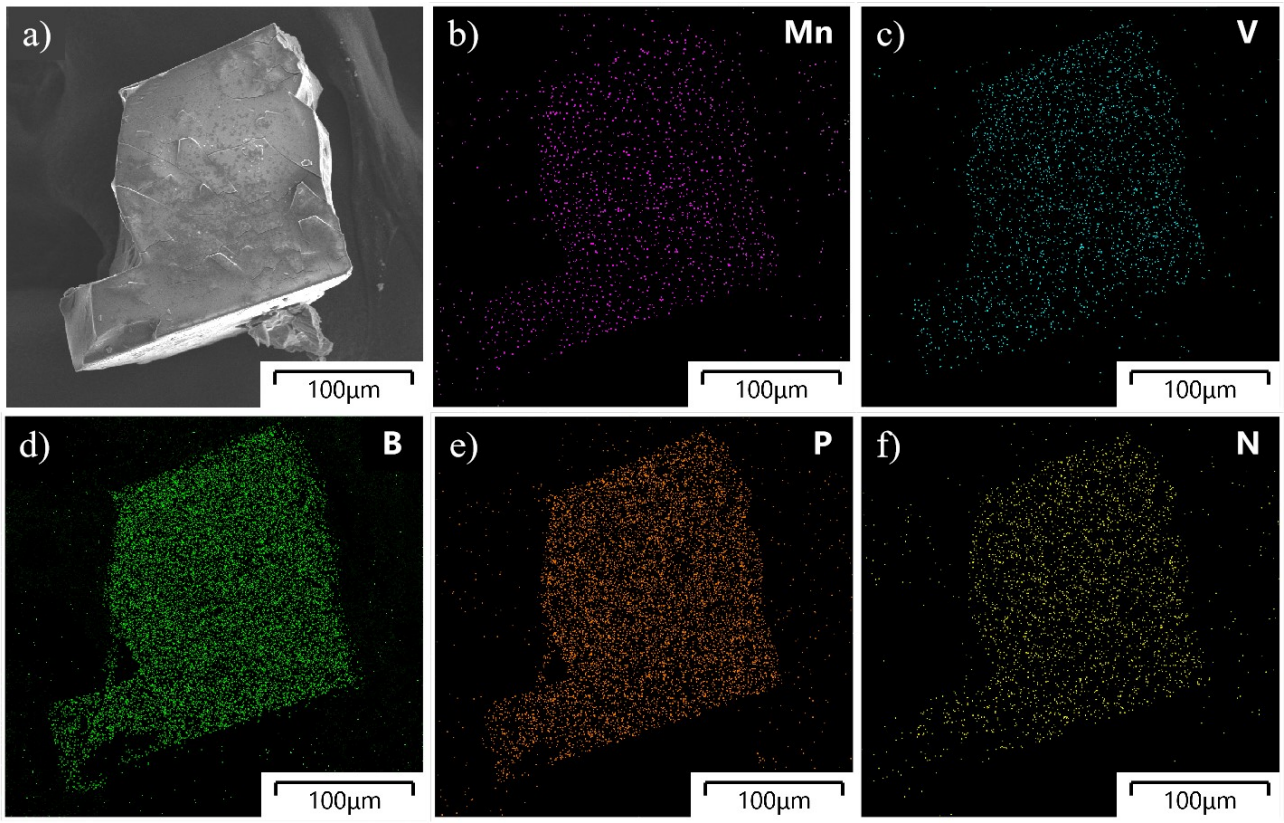

Fig. S5 (a) SEM micrograph image of **2**. (b-f) EDX mapping images of **2**.

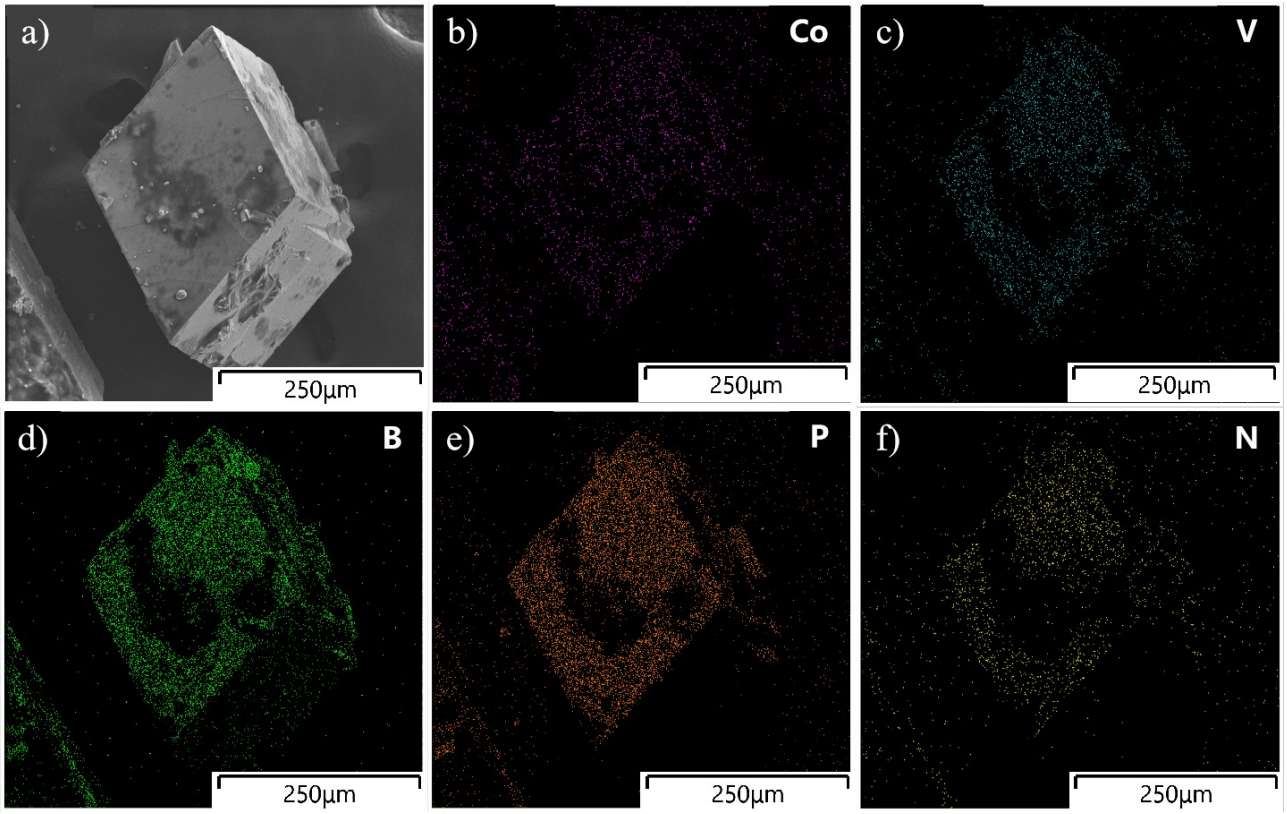

Fig. S6 (a) SEM micrograph image of **3**. (b-f) EDX mapping images of **3**.

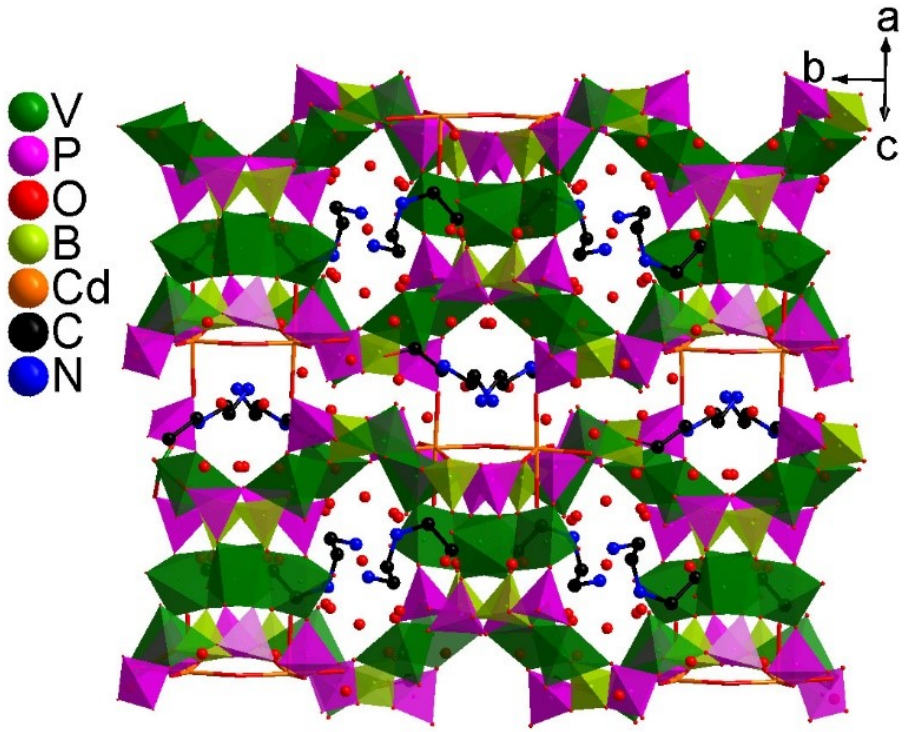

Fig. S7. The crystal packing diagram of **1**, showing 3-D $V_{12}B_6P_{12}$-1, protonated H_2aeae^{2+} cations, H_3O^+ cations and free H_2O molecules.

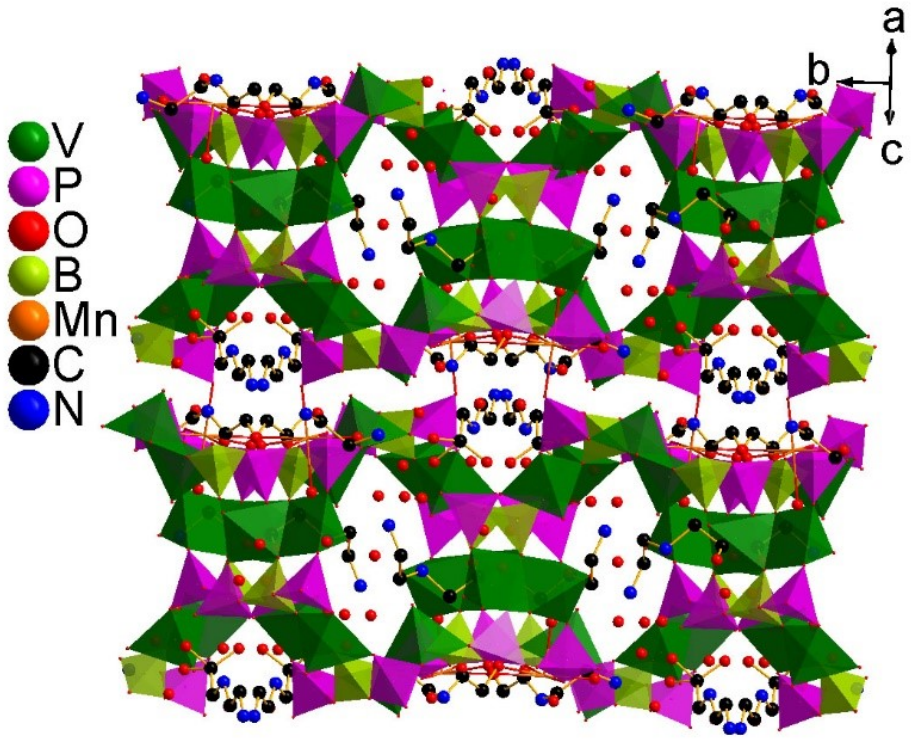

Fig. S8. The crystal packing diagram of **2**, showing 3-D $V_{12}B_6P_{12}$-2, protonated H_2aeae^{2+} cations, H_3O^+ cations and free H_2O molecules.

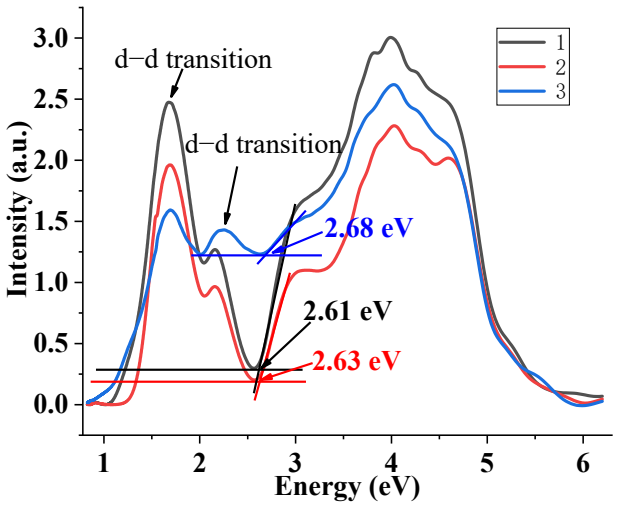

Fig. S9. UV-vis absorption spectra of **1-3**, showing absorption edges.

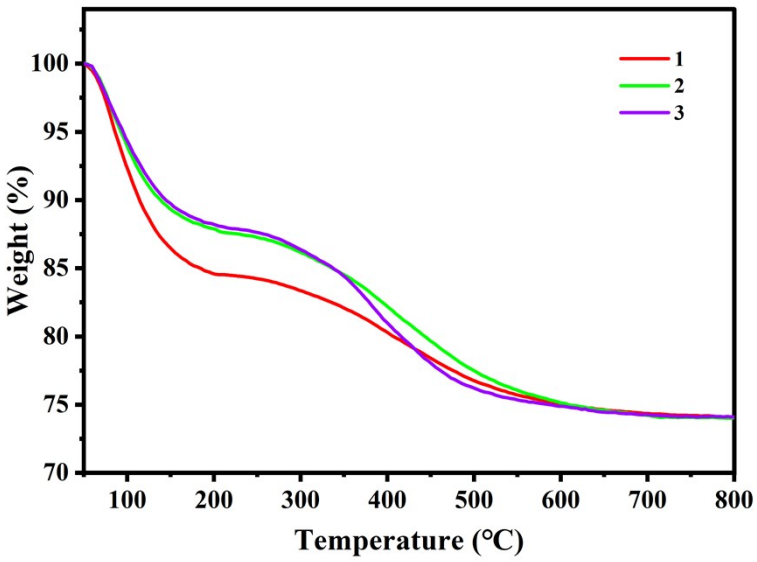

Fig. S10. TGA curves of **1**-**3**.

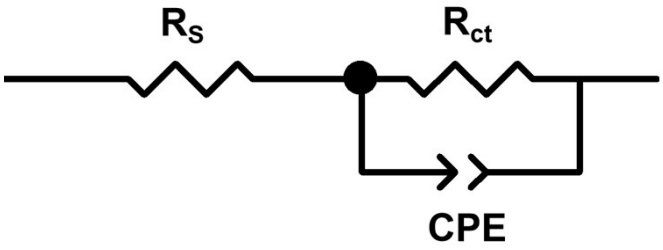

Fig. S11. The equivalent circuit diagram.

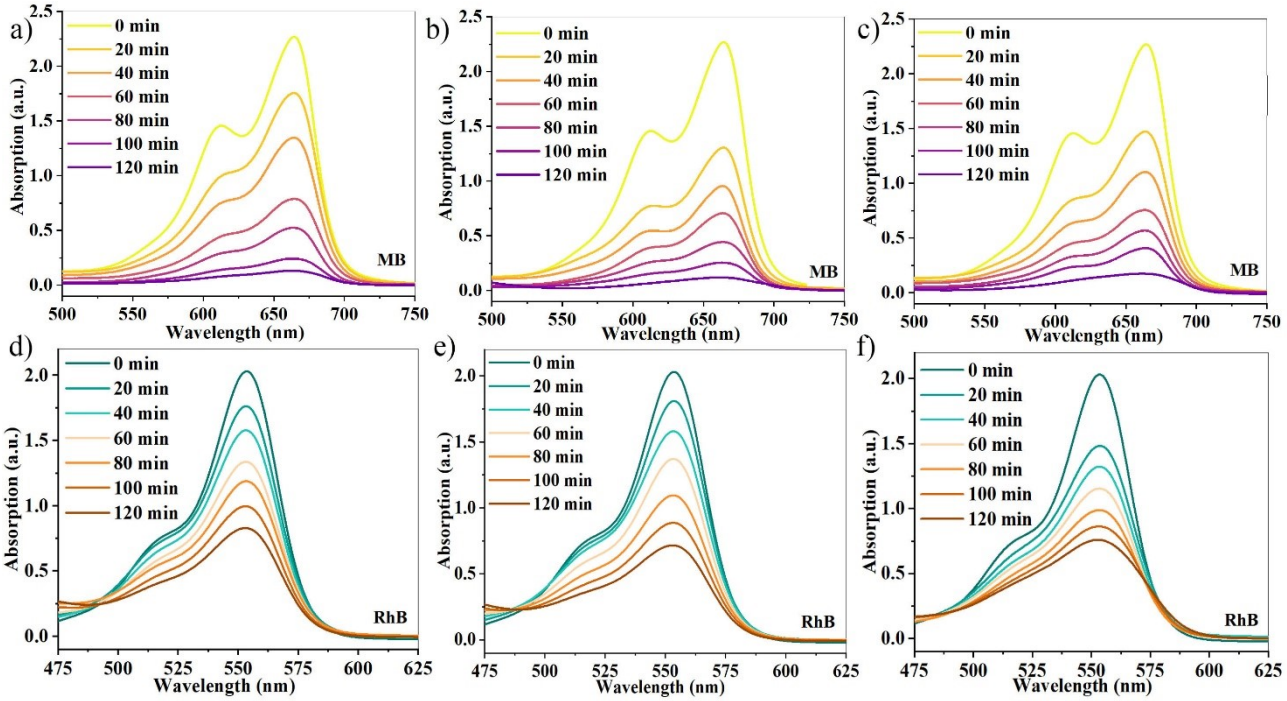

Fig. S12. UV-visible absorption spectral changes for the MB solutions at various irradiation times in the

presence of **1** (a), **2** (b) and **3** (c). UV-visible absorption spectral changes for the RhB solutions at various irradiation times in the presence of **1** (d), **2** (e) and **3** (f).

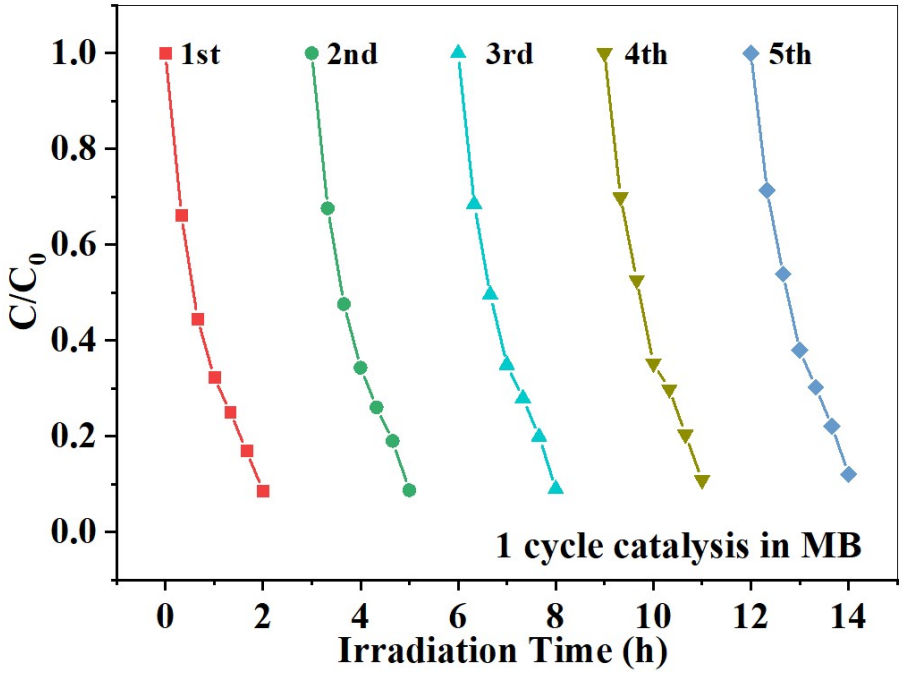

Fig. S13. Cyclic stability of **1** in MB after five test cycles.

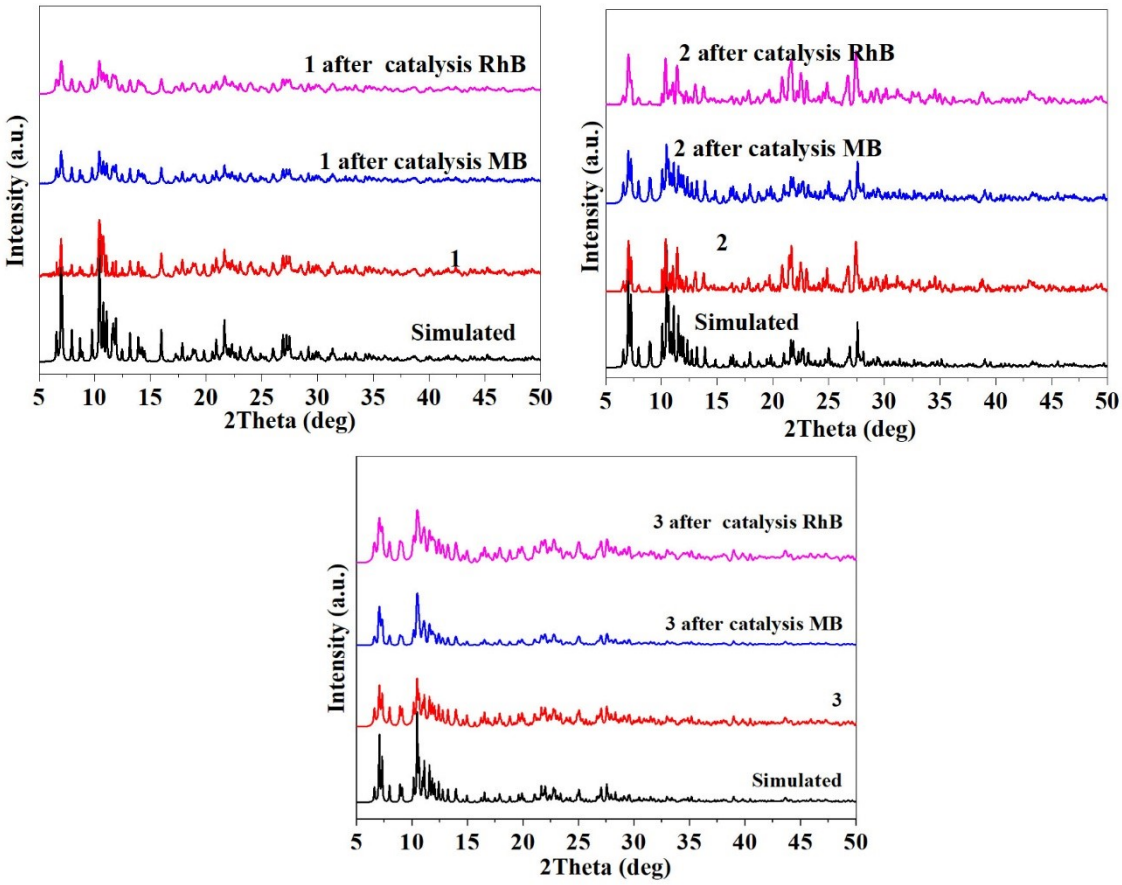

Fig. S14. PXRD patterns of **1**, **2** and **3** before and after the photo-catalysis at room temperature.

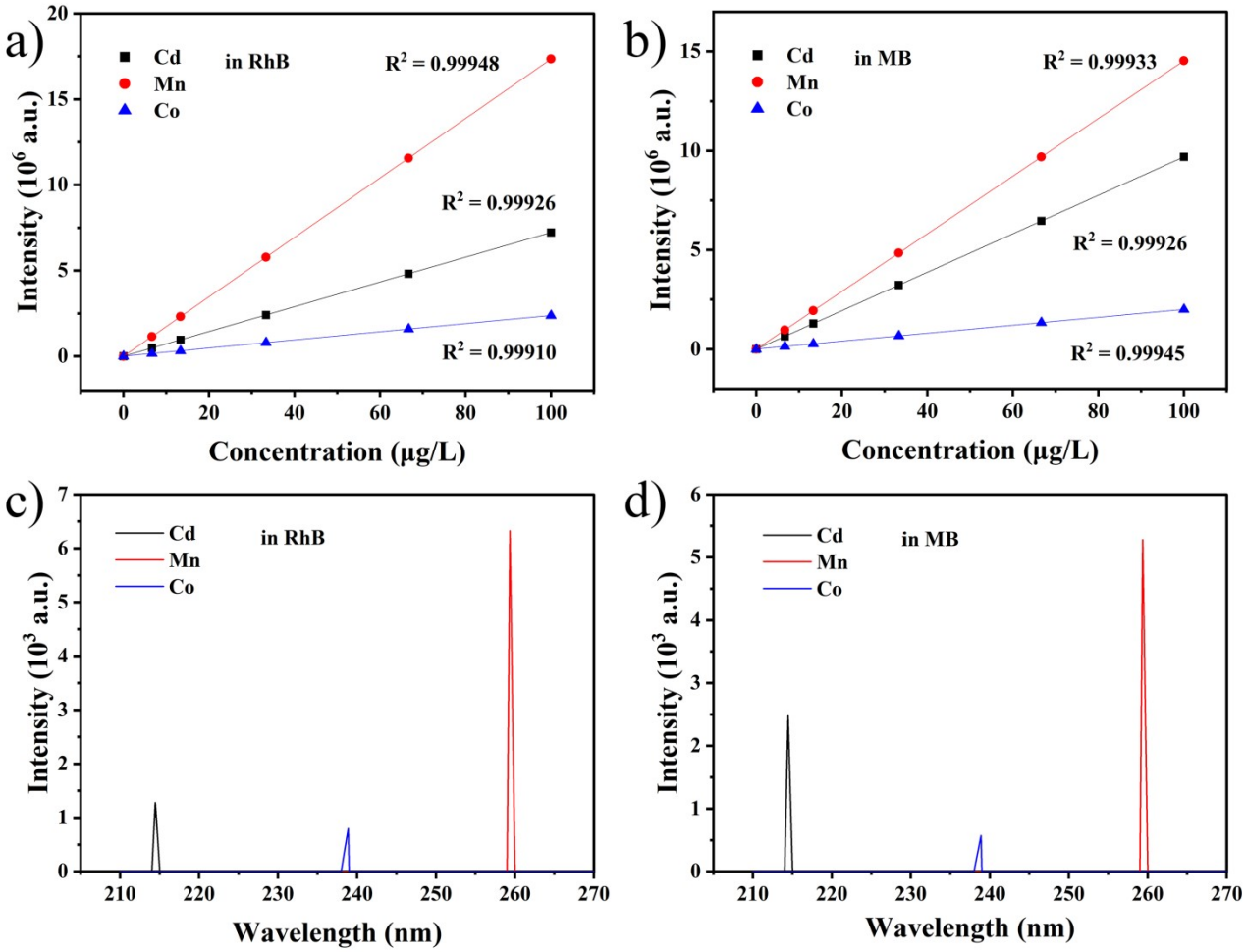

Fig. S15. The linear fit of Cd, Mn and Co to their concentration in RhB (a) and MB (b). The ICP-OES characteristic spectra of Cd, Mn and Co in RhB (c) and MB (d).

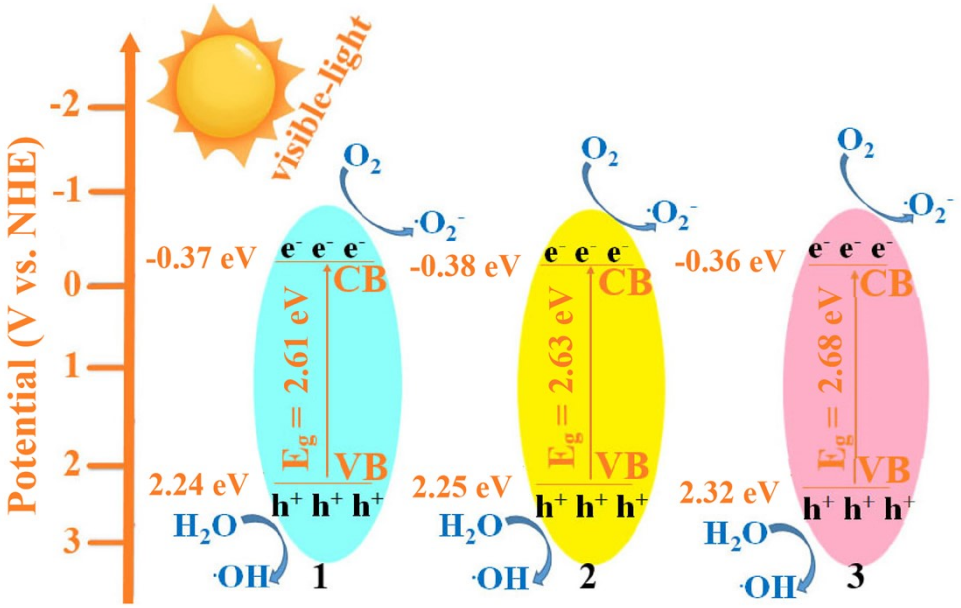

Scheme S1. Schematic diagram for energy band of **1**-**3** and degradation mechanism of contaminants by **1**-**3**.

Magnetic properties. The variable-temperature magnetic susceptibilities of **2** and **3** were measured in the temperature range of 2–300 K under an applied magnetic field of 1000 Oe (Fig. S16). At 300 K, for **2**, the $\chi_M T$ values are 13.23 cm^3 mol^{-1} K, which is slightly lower than the theoretical value of 12 uncoupled V(IV) ions (4.5 cm^3 K mol^{-1} with $S = 1/2$, $g = 2.0$) and two uncoupled Mn(II) (8.75 cm^3 K mol^{-1} with $S = 5/2$, $g = 2.0$). As the temperature decreases, the $\chi_M T$ value exhibits a decrease and then falls to a minimum value of 8.92 cm^3 mol^{-1} K at 2 K, indicating antiferromagnetic behaviors. For **3**, the $\chi_M T$ values are 8.15 cm^3 mol^{-1} K, which are lower than the theoretical value of 12 uncoupled V(IV) ions and two uncoupled Co(II) (3.75 cm^3 K mol^{-1} with $S = 3/2$, $g = 2.0$). As the temperature decreases to 2 K, the $\chi_M T$ values decrease smoothly to 0 cm^3 K mol^{-1}. The features of these curves demonstrate dominant antiferromagnetic interactions between the V(IV) ions and Co(II) ions in **3**. The magnetic behavior coincided with their similar structures ($V_{12}Mn_2$ and $V_{12}Co_2$). In the case of **3**, the intramolecular Co(II)···Co(II) distance was found to be beyond 9.5 Å (Fig. S17), and Co(II)···V(IV) distance also beyond 5 Å, therefore, effective super-exchange interaction between the metal centers was expected to be weak. The short neighboring V1···V2, V3···V4, and V5···V6 distance in **3** is 3.037 Å, 3.040 Å, and 3.048 Å, respectively, and lies in the range expected for weak antiferromagnetic coupling.[S1]

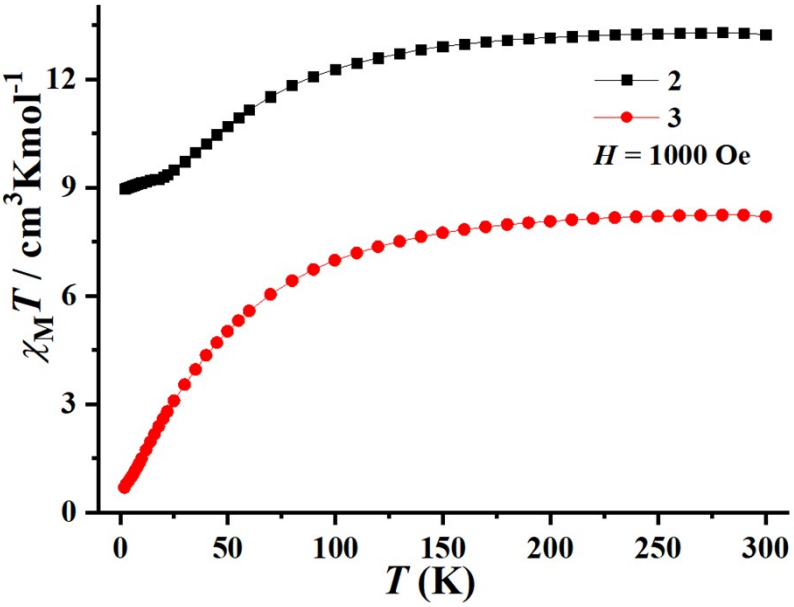

Fig. S16. $\chi_M T$ versus T for **2** and **3**.

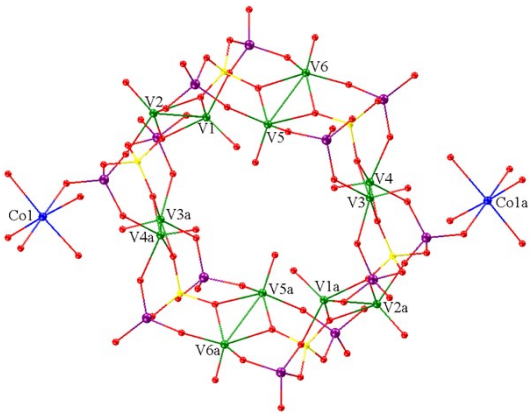

Fig. S17. The structure of $V_{12}Co_2$.

Table 1 Crystallographic data for **1**, **2** and **3**.

	1(CCDC 2360357)	**2**(CCDC 2360359)	**3**(CCDC 2360358)
Formula	$C_{12}H_{108}O_{104}N_6V_{12}B_6P_{12}Cd_2$	$C_{16}H_{102}O_{96}N_8V_{12}B_6P_{12}Mn_2$	$C_{16}H_{102}O_{96}N_8V_{12}B_6P_{12}Co_2$
Formula weight	3273.61	3100.67	3108.66
Crystal system	Monoclinic	Monoclinic	Monocnilic
Space group	$P2_1/n$	$P2_1/n$	$P2_1/n$
a, Å	16.3424(12)	16.2278(6)	16.1668(16)
b, Å	19.4148(16)	19.9186(8)	19.928(2)
c, Å	17.4299(13)	17.1067(7)	17.0811(19)
β, °	108.437(2)	107.7390(10)	108.145(4)
V, Å^3	5246.4(7)	5266.6(4)	5229.3(10)
Z	2	2	2
T, K	296(2)	296(2)	296(2)
μ, mm^{-1}	1.732	1.554	1.639
$\rho_{calcd.}$, g·cm^{-3}	2.018	1.953	1.972
F(000)	3132	3034	3026
2*θ*(max), deg	50.05	50.48	50.48
Total reflns collected	36040	48598	79454
Unique reflns	9232	12844	12939
No. of param	769	829	829
*R*1[*I*>2σ(*I*)]	0.0961	0.0602	0.0665
*wR*2(all data)	0.2900	0.1910	0.2111
GOOF on F^2			

	1.080	0.971	1.101

Table S2 The refined lattice parameters and reliability factors made by PXRD data at room temperature.

	1	**2**	**3**
Crystal system	Monoclinic	Monoclinic	Monoclinic
Space group	$P2_1/n$	$P2_1/n$	$P2_1/n$
a, Å	16.377(2)	16.259(7)	16.373(8)
b, Å	19.395(7)	19.935(6)	19.473(10)
c, Å	17.479(5)	17.097(6)	17.002(3)
β, °	105.285(13)	107.674(10)	108.858(19)
V, Å^3	5471.7(8)	5210.5(3)	5146.8(3)
Z	2	2	2
T, K	296(2)	296(2)	296(2)
$R_1[I>2\sigma(I)]$	0.0754	0.0672	0.0681
wR_2(all data)	0.2189	0.2105	0.2071

Reference

[S1] L. Huang, C. Ouyang, X. Liu, J. Zhou, H.H. Zou, H. Yuan and D. Wen, *Dalton Trans.*, 2021, **50**, 15224.